

Channel Estimation Assisted Bistatic Localization in Terrestrial and Non-Terrestrial Networks

Kunlun Li, Member, IEEE, Chao Zhang, Member, IEEE, Mohammed El-Hajjar, Senior Member, IEEE, Chao Xu, Senior Member, IEEE, Lajos Hanzo, Life Fellow, IEEE,

¹ School of Electronics and Computer Science, University of Southampton, SO17 1BJ Southampton, U.K.

CORRESPONDING AUTHOR: LAJOS HANZO (e-mail: lh@ecs.soton.ac.uk).

The financial support of the following Engineering and Physical Sciences Research Council (EPSRC) projects is gratefully acknowledged: Platform for Driving Ultimate Connectivity (TITAN) (EP/X04047X/1; EP/Y037243/1); Robust and Reliable Quantum Computing (RoarQ, EP/W032635/1); PerCom (EP/X012301/1); India-UK Intelligent Spectrum Innovation ICON UKRI-1859.

ABSTRACT Low-Earth-orbit (LEO) satellites are regarded as a key enabler for 6G communications and localization, due to their large coverage beyond conventional terrestrial networks. In this paper, we propose a downlink LEO base station (BS) bistatic localization framework relying on hybrid beamforming that alleviates the reliance on ultra-fine angle estimation by jointly exploiting time-frequency-spatial observations. A multiple-measurement-vector (MMV) based sparse model is constructed for attaining accurate channel gains and angles from limited pilots and moderate array sizes, where a modified block orthogonal matching pursuit (BOMP) algorithm is proposed to enhance robustness under highly correlated sensing matrices for localization purposes. After geometry-based timing-advance and Doppler pre-compensation at the BS, a two-dimensional (2D) upsampling matched filter having fine delay-Doppler grids is applied to estimate the residual time of arrival (ToA) and Doppler frequency. Then, the final user equipment (UE) position is obtained by intersecting the BS-centered angle-of-arrival (AoA) ray with a bistatic-range ellipse derived from the residual delay. The numerical results under realistic LEO-BS bistatic scenarios demonstrate that the proposed scheme achieves meter-level localization accuracy and highlight the performance gains attained by increasing the number of pilot symbols, subcarriers, and angular resolutions.

INDEX TERMS localization/positioning, channel estimation, low earth orbit, non-terrestrial network.

1	Nomenclature	MIMO Multiple-input multiple-output	21
2	AMP Approximate message passing	MMV Multiple measurement vector	22
3	AoA Angle-of-arrival	NLoS Non-line-of-sight	23
4	AoD Angle-of-departure	NR New radio	24
5	AWGN Additive white Gaussian noise	NTN Non-terrestrial network	25
6	BOMP Block orthogonal matching pursuit	OFDM Orthogonal frequency division multiplexing	26
7	BS Base station	OMP Orthogonal matching pursuit	27
8	CE Channel estimation	OTFS Orthogonal time frequency space	28
9	CoSaMP Compressive sampling matching pursuit	RC Receive combining	29
10	CSI Channel state information	RCS Radar cross section	30
11	DL Downlink	RF Radio frequency	31
12	DPC Doppler pre-compensation	RIS Reconfigurable intelligent surface	32
13	EIRP Effective isotropic radiated power	RMSE Root mean squared error	33
14	GNSS Global navigation satellite system	RSMA Rate splitting multiple access	34
15	IoT Internet of things	SAGIN Space-air-ground-integrated networks	35
16	ISAC Integrated sensing and communications	SMV Single measurement vector	36
17	JRC Joint radar communication	SNR Signal-to-noise ratio	37
18	LEO Low-earth-orbit	TA Timing advance	38
19	LMMSE Linear minimum mean square error	TN Terrestrial network	39
20	LoS Line-of-sight	ToA Time-of-arrival	40

41	TPC	Transmit precoding
42	UE	User equipment
43	UPA	Uniform planar array

44 I. Introduction

45 As global communication demand escalates, conventional
 46 terrestrial networks (TN) face limitations in coverage, ser-
 47 vice reliability, and resource utilization, which require im-
 48 provements for next-generation systems [1]. Non-terrestrial
 49 networks (NTN) relying on low-earth-orbit (LEO) satellites
 50 offer coverage, geometry and waveform reuse that comple-
 51 ment terrestrial 6G systems [2]–[4]. Localization in 6G plays
 52 an important role in applications such as emergency services,
 53 logistics, and autonomous driving [5], [6]. While global nav-
 54 igation satellite systems (GNSS) serve as the gold standard
 55 for outdoor positioning with high accuracy in open-sky con-
 56 ditions, their performance degrades significantly in GNSS-
 57 challenged environments, such as deep urban canyons, in-
 58 doors, or areas suffering from severe signal blockage [7].
 59 In these scenarios, satellite visibility is often limited, and
 60 multi-path effects are severe. Consequently, LEO satellites,
 61 having high transmit power and dense constellations, offer a
 62 promising complementary solution [8].

63 The GNSS constellations are designed to ensure the simul-
 64 taneous visibility of at least four satellites for trilateration
 65 [9]. LEO satellites might be viewed as a potential design
 66 alternative, but owing to their low altitude and high velocity,
 67 they exhibit a short service window for a specific user [10].
 68 Nonetheless, exploiting angle-of-arrival (AoA) information
 69 alongside propagation delay is worth investigating in the
 70 context of instantaneous and single-satellite localization. In
 71 this case, the long propagation distance and substantial delay
 72 make precise positioning heavily reliant on high-accuracy
 73 angle estimates in the single-LEO satellite scenario, which
 74 is challenging for both signal processing and hardware,
 75 especially for the calibration of large arrays, phase noise
 76 mitigation, and synchronization [11], [12].

77 From a system perspective, recent surveys have estab-
 78 lished the architectural role of NTN in 6G, highlighting
 79 multi-layer space–air–ground integration, 3GPP standardiza-
 80 tion progress, and the benefits of LEO constellations in terms
 81 of latency and rate [13]–[15]. NTN-based 6G localization has
 82 been surveyed in [5], where the authors discuss how LEO
 83 satellites can provide favourable geometry and global visibil-
 84 ity, while also identifying stringent synchronization, Doppler
 85 compensation, and joint TN–NTN design as key challenges.
 86 More broadly, ground–air–space localization has been treated
 87 in the tutorial [13], which provides a unified view of radio-
 88 based positioning across terrestrial, aerial, and satellite seg-
 89 ments, quantifying the sensitivity of the localization accuracy
 90 to system geometry and signal design. Specifically, LEO-
 91 based sensing and localization has recently attracted much
 92 attention [5], [16]–[22]. In [16], satellite based Internet-
 93 of-Things (IoT) localization is achieved via joint Doppler
 94 and angle-of-arrival estimation. In [17], [18], methods are
 95 proposed to mitigate strong LEO-induced Doppler in 5G-
 96 NTN receivers. Blind Doppler tracking relying on broadcast
 97 orthogonal frequency division multiplexing (OFDM) LEO

signals without a dedicated navigation payload has been
 demonstrated in [21]. Robust and risk-aware LEO beam-
 forming under channel and position uncertainty has been
 investigated in [20], while the fundamentals and performance
 limits of LEO-based localization have been established in
 [22]. These works confirm that LEO-based localization is
 feasible, but they often assume high-quality angle estimates
 or rely on satellite-side processing having stringent hardware
 and calibration requirements.

Accurate channel estimation (CE) is vital for both high-
 throughput communication and precise positioning [23]–
 [27]. However, LEO channels are strongly time-varying
 and Doppler-dominated, which renders conventional pilot-
 based schemes inefficient. Massive multiple-input multiple-
 output (MIMO) OFDM channel estimation tailored to LEO
 satellite communications has been developed in [24], where
 a geometry-dependent wideband channel model is combined
 with a two-stage estimation framework that exploits the
 sparsity and structured time–frequency correlation of LEO
 channels. To deal with severe Doppler and time selectivity,
 orthogonal time frequency space (OTFS)-based LEO systems
 have been studied in [28], which proposes joint Bayesian
 channel estimation and data detection in the delay–Doppler
 domain. In the context of massive IoT, grant-free random ac-
 cess and user-activity detection combined with joint channel
 estimation have been conceived for LEO-enabled networks
 [25], where a message-passing-based algorithm leverages the
 sporadic and sparse nature of user activity. To mitigate chan-
 nel aging and reduce pilot overhead, block-based Kalman
 channel tracking for LEO massive MIMO has been proposed
 in [29]. Furthermore, integrated sensing and communications
 (ISAC) frameworks have been developed in [19] for massive
 MIMO LEO, where the same waveform is exploited for
 both data transmission and parameter estimation. Overall,
 these works demonstrate that (i) exploiting the typical LEO
 propagation scenario (e.g., geometry, sparsity, and two-time-
 scale variations) and (ii) jointly designing communication
 and sensing functionalities are crucial for achieving ro-
 bust CSI and high-accuracy positioning. Nevertheless, most
 schemes are monostatic and satellite-centric, and they usually
 assume that fine angular resolution and sophisticated signal
 processing are available at the satellite or user terminals,
 which may not be practical for reasons of cost- and power-
 constraints.

To elaborate, bistatic and multistatic sensing has emerged
 as a powerful solution for exploiting the distributed nature
 of wireless networks [30]. Classical bistatic radar and
 localization frameworks provide fundamental insights into
 ellipse-based range geometry, synchronization, and target
 localization based on bistatic measurements. It has also
 been shown that terrestrial systems using OFDM based joint
 radar–communication (JRC) architectures and 5G NR-based
 sensing can be reused for range–Doppler estimation with
 the aid of appropriate synchronization and frame design
 [31]. Recent research on multistatic ISAC further exploited
 cooperation among multiple base stations or access points
 to enhance sensing coverage and robustness [32]–[35]. For
 example, RIS-aided bistatic ISAC has been studied in [32],

156 where a reconfigurable intelligent surface (RIS) supports a
 157 bistatic link between a communication transmitter and a
 158 separate sensing receiver, relying on low-cost components.
 159 Cellular-network-based multistatic ISAC architectures that
 160 reuse existing base-station deployments for cooperative sens-
 161 ing have been investigated in [33].

162 In the LEO context, bistatic ISAC frameworks exploiting
 163 separated radar receivers have been proposed in [34], [35],
 164 where rate-splitting multiple access (RSMA) is employed to
 165 manage interference, while satisfying demanding communi-
 166 cation and sensing constraints. Space-air-ground integrated
 167 bistatic sensing architectures, have also been explored [36],
 168 in which LEO, aerial platforms, and terrestrial nodes jointly
 169 participate in sensing. Existing bistatic LEO investigations,
 170 however, largely focus on target detection and communi-
 171 cation-sensing trade-offs, rather than on user-centric localiza-
 172 tion relying on TN-NTN cooperation.

173 Existing LEO localization studies are monostatic and
 174 satellite-centric [16], [19]–[22], often assuming either fine
 175 angular resolution or sophisticated signal processing [11],
 176 [12]. The associated LEO channel estimation techniques tend
 177 to exploit sparsity and geometry but they do not readily allow
 178 the translation of the recovered parameters into a single-
 179 LEO satellite bistatic positioning pipeline, while obeying
 180 an explicit geometric constraint [24]. On the other hand,
 181 the bistatic/multistatic ISAC literature tends to focus mainly
 182 on the detection issues or on the sensing-communication
 183 trade-offs [34], rather than on user-centric localization under
 184 hybrid beamforming relying on symbol-by-symbol based
 185 projections. Given the above knowledge gaps, we intrinsically
 186 amalgamate LEO-specific channel estimation in the
 187 TN-NTN cooperation in the face of bistatic range-angle
 188 constraints in a unified localization architecture. In particular,
 189 the large altitude gap between LEO satellites and the ground
 190 implies long propagation distances and substantial delays.

191 To elaborate, we consider a bistatic localization sys-
 192 tem to reduce the reliance on ultra-fine angular resolution.
 193 Specifically, we propose a joint TN-NTN bistatic downlink
 194 architecture, where the LEO satellite serves as the transmitter
 195 providing wide coverage, while a terrestrial base station
 196 (BS) acts as the receiver and performs low-latency signal
 197 processing and localization. By jointly exploiting the time-
 198 frequency observations and the associated bistatic geometric
 199 constraints, the proposed framework enables robust high-
 200 accuracy localization both for moderate array sizes and under
 201 practical hardware requirements. In particular, the LEO
 202 satellite transmits downlink pilots and each vehicular user
 203 equipment (UE) is modelled as a non-cooperative scatterer
 204 characterized by its radar cross section (RCS), generating a
 205 bistatic return received at the BS.

206 By stacking the observations across the time-frequency
 207 pilot grids, the BS formulates a sparse joint time-frequency-
 208 spatial multiple measurement vector (MMV) model for
 209 channel-parameter recovery under hybrid beamforming. In
 210 contrast to classical MMV formulations that assume a com-
 211 mon sensing matrix, the sensing matrix in our setup is
 212 symbol-dependent due to harnessing symbol-specific pre-
 213 coders/combiners. We therefore develop a modified block

orthogonal matching pursuit (BOMP) that coherently ag-
 214 gregates correlations across time-frequency snapshots under
 215 time-varying sensing matrices. Building upon the recovered
 216 angular information, we then estimate the target-specific
 217 residual delay and Doppler via a two-dimensional (2D)
 218 matched filter, and finally obtain the UE position by com-
 219 bining the estimated angle and residual time of arrival (ToA)
 220 with an elliptic bistatic range constraint. Our contributions
 221 are boldly contrasted to the state-of-the-art in Table 2, and
 222 details are listed as follows: 223

- **System model:** We propose a unified LEO-UE-BS 224
 bistatic downlink localization framework in which the 225
 LEO satellite transmits pilots and the terrestrial BS 226
 performs localization, without relying on the ultra-fine 227
 angular resolution by leveraging time-frequency diver- 228
 sity, while satisfying the associated bistatic geometric 229
 constraints. 230
- **Algorithmic approach:** We formulate a sparse joint 231
 time-frequency-spatial MMV channel parameter es- 232
 timation problem under hybrid beamforming, where 233
 the sensing matrix is symbol-dependent. To address 234
 this, we develop a modified BOMP that coherently 235
 aggregates correlations across time-frequency snapshots 236
 under time-varying sensing matrices and mitigates the 237
 impact of highly correlated dictionaries. 238
- **Localization phase:** We exploit the known LEO-BS 239
 geometry to perform timing advance and Doppler pre- 240
 compensation, so that the residual ToA and Doppler 241
 become target-specific. We then apply 2D matched 242
 filtering for estimating the residual delay-Doppler pair 243
 and combine it with the angle estimate via an explicit 244
 elliptic bistatic range constraint to infer the UE position. 245
- **Validation:** Numerical results validate the proposed 246
 framework under realistic LEO-BS bistatic settings, 247
 demonstrating meter-level localization accuracy and 248
 illustrating the impact of pilot symbols/subcarriers 249
 allocation and angular resolution on localization 250
 robustness. 251

252 To the best of our knowledge, such a bistatic LEO
 253 based localization system using an MMV model and elliptic
 254 constraints has not been studied in the open literature. A
 255 list of main variables is included in Table 1. This paper is
 256 organized as follows: Section II introduces the system model.
 257 Our time-frequency-spatial MMV formulation is derived in
 258 Section III. Moreover, the system parameter setting and
 259 simulation results are investigated in Section IV. Finally, our
 260 conclusions are provided in Section V. 261

262 *Notations:* a , \mathbf{a} , \mathbf{A} stand for scalar, vector and matrix,
 263 respectively. \mathbf{A}^T , \mathbf{A}^H , \mathbf{A}^\dagger , $\|\mathbf{a}\|_2$ and $\|\mathbf{A}\|_F$ denote the
 264 transpose, Hermitian transpose, pseudoinverse, the Euclidean
 265 norm of vector \mathbf{a} , and the Frobenius norm of matrix \mathbf{A} ,
 266 respectively. The (i, j) -th entry of \mathbf{A} is $[\mathbf{A}]_{i,j}$, and $\text{diag}(\mathbf{a})$
 267 is a diagonal matrix formed by the diagonal elements of \mathbf{a} .
 268 $\mathbb{E}(\mathbf{A})$ is the expectation of \mathbf{A} , $\text{vec}(\mathbf{A})$ is the vectorization
 269 operation of \mathbf{A} , $\text{mod}(i, j)$ denotes the modulo operation, and
 270 $j = \sqrt{-1}$; $(\mathbf{A})^*$ represents the conjugate of matrix \mathbf{A} .

TABLE 1: List of Main Variables

Symbol	Description	Symbol	Description
c	Speed of light	f_c	Carrier frequency
λ	Wavelength, $\lambda = c/f_c$	f_s	Subcarrier spacing
N_{sc}	Number of OFDM subcarriers	T	OFDM symbol duration, $T = 1/f_s$
M_s	Number of pilot OFDM symbols	P	Number of time-frequency snapshots, $P = M_s N_{sc}$
N_t	Number of LEO transmit antennas	N_t^x, N_t^y	LEO transmit UPA size along x/y axes
N_r	Number of BS receive antennas	N_r^x, N_r^y	BS receive UPA size along x/y axes
N_{rf}	Number of RF chains	K	Number of UEs
L_p	Number of propagation paths	\mathbf{p}_{LEO}	Position of LEO
\mathbf{p}_{BS}	Position of BS	\mathbf{p}_k	Position of k -th UE
$\theta_{k,l}^x, \theta_{k,l}^y$	Path angles on the x/y axes	\mathbf{v}_t	LEO transmit array response
\mathbf{v}_r	BS receive array response	τ_l	Delay of l -th path
v_l	Doppler shift of l -path	τ_l^{res}	Residual delay after timing advance (TA)
v_l^{res}	Residual Doppler after Doppler pre-compensation (DPC)	$g_{k,l}$	Complex path gain
\mathcal{P}_{PL}	Path-loss power gain	\mathcal{P}_{abs}	Atmospheric absorption transmittance
\mathcal{P}_{ref}	Reflection loss coefficient for NLoS paths	$\mathbf{H}_{k,m,n}$	MIMO channel for k -th UE at symbol m , subcarrier n
\mathbf{F}_m	LEO transmit precoder at m -th symbol	\mathbf{W}_m	BS receive combiner at m -th symbol
$\mathbf{s}_{k,m,n}$	Pilot vector of k -th UE on (m,n) -th snapshot	$\mathbf{y}_{m,n}$	Received BS signal on (m,n) -th snapshot
$\mathbf{z}_{m,n}$	AWGN vector	$\phi_{m,i}$	Sensing row for RF chain i at symbol m
Φ_m	Stacked sensing matrix	$\mathbf{A}_t, \mathbf{A}_r$	Transmit/receive angular dictionaries
Γ	Kronecker angular dictionary, $\Gamma = \mathbf{A}_r \otimes \mathbf{A}_t$	Ψ_m	Snapshot-based sensing matrix at m -th symbol
$\mathbf{h}_{m,n}$	Sparse angular-domain channel vector	S	Joint sparse support across P snapshots
$S(g)$	MMV score for atom g in modified BOMP	\mathbf{S}	Time-frequency coefficient matrix for a selected atom
$\mathbf{a}_t(v)$	Temporal steering vector on Doppler grid	$\mathbf{a}_f(\tau)$	Frequency steering vector on delay grid
$C(v, \tau)$	2D matched-filter response	$\hat{v}^{\text{res}}, \hat{\tau}^{\text{res}}$	Estimated residual Doppler and delay
$\hat{\boldsymbol{\mu}}_r$	Estimated BS-side direction vector	$\mathbf{p}(s)$	BS-centered ray, $\mathbf{p}(s) = \mathbf{p}_{BS} + s\hat{\boldsymbol{\mu}}_r$
D	Total bistatic range, $D = \ \mathbf{p}_{LEO} - \mathbf{p}_{BS}\ + c\hat{\tau}^{\text{res}}$		

271 II. System Model

272 Our space-air-ground-integrated networks (SAGIN) include a
 273 MIMO LEO satellite, a ground BS and K vehicular UE. We
 274 consider a downlink (DL) OFDM based LEO-UE-BS bistatic
 275 localization scenario relying on hybrid transmit precoding
 276 (TPC) and receive combining (RC) at the LEO transmitter
 277 and the BS receiver, respectively, where the vehicular UEs
 278 are the targets. The LEO and BS adopt uniform planar arrays
 279 (UPAs) of sizes $N_t = N_t^x N_t^y$ and $N_r = N_r^x N_r^y$, respectively,
 280 both lying on the xy -plane and pointing to the $+z$ half-
 281 space. Specifically, we assume that the subcarrier spacing is
 282 f_s and N_{sc} subcarriers are employed. The symbol duration
 283 is $T = 1/f_s$, while a pilot frame contains M_s OFDM pilot
 284 symbols, yielding $P = M_s N_{sc}$ snapshots per frame.

285 As illustrated in Fig. 1, the position and velocity of
 286 the LEO is inferred by the ground BS using the satellite
 287 calendar, denoted as $\mathbf{p}_{LEO} = [p_{LEO}^x, p_{LEO}^y, p_{LEO}^z]^T$ and
 288 $\dot{\mathbf{p}}_{LEO} = [\dot{p}_{LEO}^x, \dot{p}_{LEO}^y, \dot{p}_{LEO}^z]^T$, respectively. The ground
 289 BS is located at $\mathbf{p}_{BS} = [p_{BS}^x, p_{BS}^y, p_{BS}^z]^T$, and these are as-
 290 sumed to be known for delay and Doppler pre-compensation
 291 [37]. Additionally, we assume that all vehicular UEs are at
 292 unknown positions, formulated as $\mathbf{p}_k = [p_k^x, p_k^y, p_k^z]^T$ with
 293 $k = 1, \dots, K$. Furthermore, we assume that the UEs are

non-cooperative targets, where the reflection characteristic 294
 is quantified by its RCS [38]. 295

A. Channel Model 296

We define the transmit UPA response for the l -th propagation 297
 path of the k -th UE, formulated as [19] 298

$$\mathbf{v}_{k,l}^x = \frac{1}{\sqrt{N_t^x}} \left[1, \exp\{-j\pi \sin \theta_{k,l}^y \cos \theta_{k,l}^x\}, \dots, \right. \\ \left. \exp\{-j\pi(N_t^x - 1) \sin \theta_{k,l}^y \cos \theta_{k,l}^x\} \right]^T, \quad (1)$$

$$\mathbf{v}_{k,l}^y = \frac{1}{\sqrt{N_t^y}} \left[1, \exp\{-j\pi \cos \theta_{k,l}^y\}, \dots, \right. \\ \left. \exp\{-j\pi(N_t^y - 1) \cos \theta_{k,l}^y\} \right]^T, \quad (2)$$

where $\theta_{k,l}^x$ and $\theta_{k,l}^y$ denote the angles on the x and y axis, res- 299
 pectively. Since the LEO is typically deployed at an altitude 300
 significantly higher than the surrounding scatterers near the 301
 users, the angle of departure (AoD) $\theta_{k,l}^t$ of the propagation 302
 paths associated with the k -th UE can be considered nearly 303
 identical, mathematically represented as $\theta_{k,l}^t \triangleq \theta_k^t, \forall l$. 304
 We drop the subscript l , and express the UPA response 305
 as $\mathbf{v}_{k,l}^t(f) = \mathbf{v}_k^t(f)$. Hence, we define $\mathbf{v}_{k,n}^t \triangleq \mathbf{v}_k^t(f_n)$. 306
 However, for the ground link between the BS and UEs, the 307

TABLE 2: Contrasting Our Novelty to the Literature

	[16]	[17]	[18]	[19]	[20]	[5]	[21]	[22]	[34]	[35]	This work
System Model											
DL NTN CE based localization				✓		✓		✓			✓
Single-satellite	✓			✓		✓					✓
LEO Bistatic sensing									✓	✓	✓
Algorithmic Approach											
Geometry-based precompensation		✓	✓								✓
Residual ToA & Doppler estimation							✓				✓
Joint time-frequency-spatial MMV											✓
Localization Phase											
Elliptic Constraints											✓

308 non-line-of-sight (NLoS) path cannot be ignored. Under the
 309 assumption of perfect time and frequency synchronization¹,
 310 the effective channel matrix $\mathbf{H}_{k,m,n} \in \mathbb{C}^{N_r \times N_t}$ for the k -th
 311 UE over the n th subcarrier of the m -th OFDM symbol is
 312 formulated as follows:

$$\mathbf{H}_{k,m,n} = \sum_{l=0}^{L_p-1} g_{k,l} e^{j2\pi(v_{l,k} t_m - \tau_{l,k} f_n)} \mathbf{v}_r(\boldsymbol{\mu}_{r,l,k}) \mathbf{v}_t(\boldsymbol{\mu}_{t,k})^H, \quad (3)$$

313 where $\tau_{l,k}$ and $v_{l,k}$ are the propagation delay and Doppler
 314 of l -th path, while $\boldsymbol{\mu}_{t,k}$ and $\boldsymbol{\mu}_{r,l,k}$ denote the transmit and
 315 receive spatial frequencies, respectively. The complex gain
 316 is denoted as $g_{k,l}$, and based on [10], it is modelled by
 317 a shadowed Rician fading distribution. The time-varying
 318 channel coefficient can be expressed as

$$g(t) = \underbrace{A(t) \exp[j\zeta(t)]}_{NLoS} + \underbrace{Z(t) \exp[j\xi]}_{LoS}, \quad (4)$$

319 where $A(t)$ follows the Rayleigh distribution with uniformly
 320 distributed phase $\zeta(t)$ and $Z(t)$ obeys the Nakagami-m
 321 distribution with a constant line-of-sight (LoS) phase ξ .
 322 Given that the average power levels of the NLoS and LoS
 323 components are $|A(t)|^2 = 2b_0$ and $|Z(t)|^2 = \Omega$, they satisfy
 324 the normalization $\Omega + 2b_0 = 1$ [10].

- **Path Loss:** The path loss gain is formulated as:

$$\mathcal{P}_{PL} = \left(\frac{c}{4\pi f_c} \right)^2 d^{-\alpha_p}, \quad (5)$$

326 where c is the speed of light, f_c is the carrier frequency
 327 and α_p is the path loss exponent.

- **Atmospheric Absorption:** Given the optical thickness η_i , a Beer-Lambert-law-based model for the transmittance is expressed as [10]:

$$\mathcal{P}_{abs}(\eta_i) = \exp\left(-\sum_i \eta_i\right). \quad (6)$$

¹The time frequency synchronization problem has been investigated in [39], which is outside the scope of this work.

Note that the value of η_i for different frequency and
 gases can be found in [40].

Therefore, the complex gain for the target LoS link is formulated as $g_{k,0} = \sqrt{\Omega \mathcal{P}_{PL} \mathcal{P}_{abs} \mathcal{P}_{RCS}}$, where \mathcal{P}_{RCS} represents the reflection power loss determined by the UE's RCS, denoted as $\sigma_{RCS,k}$. In addition, the power gain of the NLoS component is expressed as $g_{k,l} = \sqrt{2b_0 \mathcal{P}'_{PL} \mathcal{P}_{abs} \mathcal{P}_{RCS} \mathcal{P}_{ref}}$, where \mathcal{P}'_{PL} denotes the path loss for the NLoS paths and \mathcal{P}_{ref} represents the additional reflection loss caused by environmental scatterers.

B. Signal Model

For the m -th pilot symbol and n -th subcarrier, the LEO applies a symbol-dependent TPC $\mathbf{F}_m \in \mathbb{C}^{N_t \times N_{rf}}$ and the BS applies a RC $\mathbf{W}_m \in \mathbb{C}^{N_r \times N_{rf}}$, where N_{rf} is the number of radio frequency (RF) chains. For each UE $k = 1, \dots, K$, the LEO transmits a unit-power pilot $\mathbf{s}_{k,m,n} \in \mathbb{C}^{N_{rf} \times 1}$ on the snapshot (m, n) .

The multiuser observation at the BS is expressed as

$$\mathbf{y}_{m,n} = \sum_{k=1}^K \mathbf{W}_m^H \mathbf{H}_{k,m,n} \mathbf{F}_m \mathbf{s}_{k,m,n} + \mathbf{z}_{m,n}, \quad (7)$$

where $\mathbf{z}_{m,n} \sim \mathcal{CN}(0, \sigma^2 \mathbf{I}_{N_{rf}})$ is the additive white Gaussian noise (AWGN).

To separate the k -th UE's signal, we assign pilots across the time-frequency set, where we enforce strict pilot orthogonality across users over the time-frequency pilot grids $\sum_{m=0}^{M_s-1} \sum_{n=0}^{N_{sc}-1} (\mathbf{s}_{k,m,n})^H \mathbf{s}_{\hat{k},m,n} = 0, \forall k \neq \hat{k}$. Equivalently, over a selected pilot subset $\mathcal{G} = \{(m_p, n_p)\}_{p=1}^{M_s N_{sc}}$ associated with $|\mathcal{G}| = M_s N_{sc}$, we have the k -th UE's receive signal after either Walsh-Hadamard or Zadoff-Chu sequences are spread across \mathcal{G} . Note that, the pilot non-orthogonality leads to multi-user interference, which has been extensively studied in the literature together with mitigation techniques, such as pilot decontamination and superimposed pilots [41], [42]. The related non-orthogonal signature based multi-user detection has also been widely investigated in compressive sensing based frameworks [43], [44]. In this paper, we focus

our attention on the strictly-orthogonal pilot allocation case to characterize the proposed bistatic localization framework. Consequently, when focusing on a single UE, we drop the UE index k and use $\sigma_{RCs,k}$, $\mathbf{H}_{m,n}$ as well as $\mathbf{y}_{m,n}$ without ambiguity.

C. Pre-Compensated Received Signal Model

Conventional delay and Doppler estimation techniques in terrestrial OFDM systems often rely on FFT/IFFT-based signal processing methods [45]. These approaches are effective under moderate mobility and short propagation delay conditions. Therefore, timing advance (TA) and Doppler pre-compensation (DPC) is required in the non-terrestrial network [37], [46]. As the distance between the BS and UE is significantly lower than that between the LEO and UE, we exploit the location of the BS in support of the TA and DPC. Thus, the receive signal can be further expressed as

$$\hat{\mathbf{y}}_{m,n} = \underbrace{\mathbf{W}_m^H \hat{\mathbf{H}}_{m,n} \mathbf{F}_m \mathbf{s}_{m,n}}_{\tilde{\mathbf{y}}_{m,n}} + \mathbf{z}_{m,n}, \quad (8)$$

where $\hat{\mathbf{H}}_{m,n} = \sum_{l=0}^{L_p-1} \alpha_l e^{j2\pi(v_l^{\text{res}} mT - \tau_l^{\text{res}} f_n)} \mathbf{v}^r(\mu_{r,l}) \mathbf{v}^t(\mu_t)^H$, and v_l^{res} , τ_l^{res} denote the residual Doppler shift and delay for the l -th path, respectively.

Furthermore, Fig. 1 illustrates the considered DL LEO-UE-BS bistatic geometry and the geometry-aided pre-compensation concept, while Fig. 2 summarizes the corresponding signal processing flow. Specifically, as depicted in Fig. 1, by exploiting the known locations of the LEO and BS, TA and DPC are performed with respect to the LEO-BS reference, resulting in the pre-compensated receive signal model in (8). This is the first step shown in Fig. 2, converting the original propagation delay/Doppler into the residual quantities τ_l^{res} and v_l^{res} , which will be estimated.

III. Problem Formulation

A. Time-Frequency-Spatial Sparsity

We assume having a single pilot frame with M_s OFDM pilot symbols and N_{sc} subcarriers, yielding $M_s N_{sc}$ snapshots. After DPC and TA with respect to the LEO-BS reference, each propagation path is characterized by a residual delay τ_l^{res} and residual Doppler v_l^{res} . For the m -th pilot symbol and the n -th subcarrier, the N_{rf} -dimensional receive signal vector at the BS is modelled as

$$\hat{\mathbf{y}}_{m,n} = \sum_{l=0}^{L_p-1} \alpha_l e^{j2\pi(v_l^{\text{res}} t_m - \tau_l^{\text{res}} f_n)} (\mathbf{W}_m^H \mathbf{B}_l \mathbf{F}_m \mathbf{s}_{m,n}) + \mathbf{z}_{m,n}, \quad (9)$$

where we have $t_m = (m-1)T$, $f_n = (n - \frac{N_{sc}-1}{2})f_s$, $\mathbf{B}_l = \mathbf{v}^r(\mu_{r,l}) \mathbf{v}^t(\mu_t)^H$, while $\mathbf{F}_m \in \mathbb{C}^{N_t \times N_{rf}}$, and $\mathbf{W}_m \in \mathbb{C}^{N_r \times N_{rf}}$ are the per-symbol hybrid beams with unit-norm columns.

Let us define the sensing row for the i -th RF chain at time m , and assume identical pilot symbols across all subcarriers, i.e. $\mathbf{s}_{m,n} = \mathbf{s}_m$. Then, we have

$$\phi_{m,i} = (s_{m,i} \mathbf{f}_{m,i}^T \otimes \mathbf{w}_{m,i}^H) \in \mathbb{C}^{1 \times (N_t N_r)}, \quad (10)$$

with $\mathbf{f}_{m,i}$ and $\mathbf{w}_{m,i}$ being the i -th columns of \mathbf{F}_m and \mathbf{W}_m , respectively. Stacking the $\phi_{m,i}$ values for $i = 1, \dots, N_{rf}$ yields

$$\Phi_m = \begin{bmatrix} s_{m,1} \mathbf{f}_{m,1}^T \otimes \mathbf{w}_{m,1}^H \\ \vdots \\ s_{m,N_{rf}} \mathbf{f}_{m,N_{rf}}^T \otimes \mathbf{w}_{m,N_{rf}}^H \end{bmatrix} \in \mathbb{C}^{N_{rf} \times (N_t N_r)}. \quad (11)$$

Then, the UPA's angular dictionaries are given by

$$\begin{aligned} \mathbf{A}_t &= [\mathbf{a}_t(\tilde{\mu}_{t,1}), \dots, \mathbf{a}_t(\tilde{\mu}_{t,G_t})], \\ \mathbf{A}_r &= [\mathbf{a}_r(\tilde{\mu}_{r,1}), \dots, \mathbf{a}_r(\tilde{\mu}_{r,G_r})]. \end{aligned} \quad (12)$$

where $\tilde{\mu}_{t,j}$ and $\tilde{\mu}_{r,j}$, $j = 1, \dots, G_t/G_r$ denote the predefined 2D spatial-frequency grids at the LEO and the BS, respectively. Since each candidate path is characterized by one point of the receive grid and the transmit grid, the corresponding joint transmit receive atom becomes separable in the vectorized domain. Therefore, the overall angular dictionary of the vectorized channel is constructed as

$$\Gamma \triangleq \mathbf{A}_r \otimes \mathbf{A}_t \in \mathbb{C}^{(N_t N_r) \times (G_r G_t)}. \quad (13)$$

Therefore, the snapshot-based sensing matrix is represented

$$\Psi_m \triangleq [\phi_{m,1} \Gamma; \dots; \phi_{m,N_{rf}} \Gamma] \in \mathbb{C}^{N_{rf} \times (G_r G_t)}, \quad (14)$$

followed by per-column ℓ_2 -normalization for stabilizing the MMV pursuit. Therefore, the stacked MMV signal at the RF receive combiner may be expressed as follows:

$$\hat{\mathbf{y}}_{m,n} = \Psi_m \mathbf{h}_{m,n} + \mathbf{z}_{m,n}, \quad (15)$$

where $\hat{\mathbf{y}}_{m,n} \in \mathbb{C}^{N_{rf} \times 1}$ represents the stacked RF chain observations and $\mathbf{h}_{m,n}$ is a $G_r G_t \times 1$ angular-domain channel vector at the (m,n) -th snapshot, whose sparse support remains unchanged during the (m,n) -th time-frequency resources after TA and DPC.

In summary, assuming identical pilots across subcarriers, the rows of the sensing matrix are defined in (10) and stacked into Φ_m in (11). With the UPA angular dictionaries in (12) and the Kronecker dictionary Γ in (13), we form the snapshot-based sensing matrix Ψ_m in (14), leading to the sparse linear model in (15). The MMV construction is illustrated as the second stage in Fig. 2.

B. Modified BOMP Assisted Location Information Recovery

Recall from (15) that each snapshot satisfies

$$\mathbf{y}_p = \Psi_{m(p)} \mathbf{h}_p + \mathbf{z}_p, \quad p = 1, \dots, P, \quad (16)$$

where we have $P = M_s N_{sc}$ snapshots indexed by p , and $\Psi_{m(p)}$ denotes the sensing matrix corresponding to the pilot symbol index $m(p)$. Owing to the in common propagation paths, all angular-domain channel vectors share the joint sparse support of:

$$\mathcal{S} = \text{supp}(\mathbf{h}_1) = \dots = \text{supp}(\mathbf{h}_P) \subset \{1, \dots, G_r G_t\}, \quad (17)$$

where supp denotes the sparse support. Before the MMV pursuit, we normalize each Ψ_m on a column by column basis to unit ℓ_2 -norm to stabilize the atom selection across heterogeneous sensing matrices. A modified BOMP is then

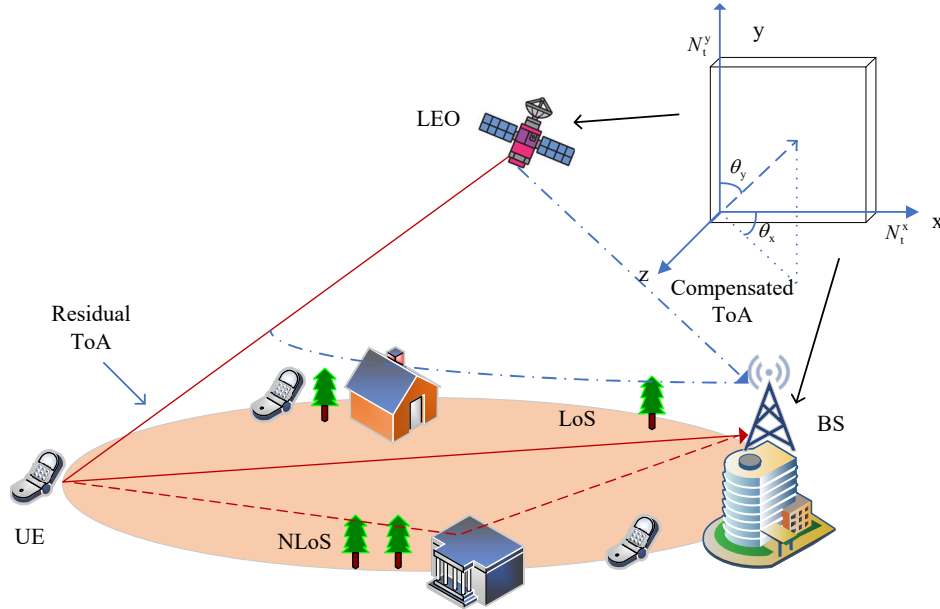


FIGURE 1: Geometry of downlink bistatic MIMO LEO based localization, where the locations of LEO and BS are known and UE is about to estimate.

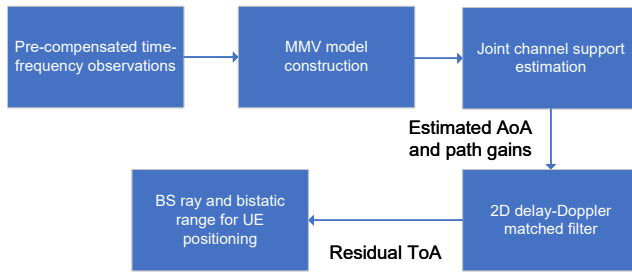


FIGURE 2: Flowchart of the proposed localization scheme using MMV model.

followed by residual update. Steps 2)-3) are then repeated until $|\mathcal{S}| = L_p$.

4) Outputs and mapping over the time-frequency grid: At convergence we obtain the joint support $\hat{\mathcal{S}} = \{g_0, \dots, g_{L_p-1}\}$ and the angular-domain coefficients $\{\hat{\mathbf{h}}_p\}_{p=1}^P$. Each index g_l uniquely maps to an AoA/AoD grid pair $(i_{r,l}, i_{t,l})$ in the receive and transmit angular dictionaries, thereby providing coarse angular estimates. For subsequent delay-Doppler processing, the coefficients associated with g_l are reshaped over the time-frequency plane into $\mathbf{S}^{(l)} \in \mathbb{C}^{M_s \times N_{sc}}$, with

$$[\mathbf{S}^{(l)}]_{m,n} = [\hat{\mathbf{h}}_{(m-1)N_{sc}+n}]_{g_l}, \quad (20)$$

harnessed for selecting L_p atoms by maximizing the sum of per-snapshot correlations over all P noisy measurements.

1) Initialization: Set $\mathcal{S} \leftarrow \emptyset$, and initialize the residuals as $\mathbf{r}_p \leftarrow \mathbf{y}_p$ for all $p = 1, \dots, P$.

2) Atom selection at iteration $t = 0, \dots, L_p - 1$: Let $\omega_{p,g} \triangleq \Psi_{m(p)}(:, g)$ be the g -th column of $\Psi_{m(p)}$, which corresponds to the g -th transmit-receive angular atom. We then quantify the MMV score of

$$S(g) = \sum_{p=1}^P |\omega_{p,g}^H \mathbf{r}_p|^2, \quad (18)$$

and select $\hat{g} = \arg \max_g S(g)$. The joint support is updated as $\mathcal{S} \leftarrow \mathcal{S} \cup \{\hat{g}\}$.

3) Least-squares (LS) update (per snapshot): For each p , we form the reduced sensing matrix $\mathbf{A}_p = \Psi_{m(p)}(:, \mathcal{S})$ and solve the per-snapshot least-squares problem of

$$\begin{aligned} \hat{\mathbf{h}}_p &= \arg \min_{\mathbf{x}} \|\mathbf{y}_p - \mathbf{A}_p \mathbf{x}\|_2^2 = \mathbf{A}_p^\dagger \mathbf{y}_p, \\ \mathbf{r}_p &= \mathbf{y}_p - \mathbf{A}_p \hat{\mathbf{h}}_p, \end{aligned} \quad (19)$$

which is then used for estimating the residual Doppler and delay pair $(\hat{\nu}_l^{\text{res}}, \hat{\tau}_l^{\text{res}})$ via the 2D matched filter of Section C. The modified BOMP procedure is summarized in Algorithm 1.

Remark: The proposed procedure can be regarded as a generalized BOMP algorithm that is specifically tailored for the heterogeneous sensing matrices arising from beamforming. Compared to BOMP with its time-varying sensing matrix, defined as Ψ_m , the classical simultaneous orthogonal matching pursuit (SOMP) has a time-invariant sensing matrix, denoted as Ψ . By contrast, in our MMV model, each snapshot p is observed through a symbol-dependent sensing matrix $\Psi_{m(p)}$ defined in (15), which reflects the varying TPCs/RCs over m . The MMV score in (18) therefore aggregates correlations across both the time- and frequency-domain, while appropriately accounting for per-symbol sensing. This joint processing exploits the fact that the physical paths remain unchanged within a pilot frame, so that even if some snapshots are heavily noise-contaminated owing to being poorly illuminated by a specific beam pattern, the

Algorithm 1 Modified BOMP for Joint Angular Support Recovery across P Snapshots

- 1: **Input:** $\{\mathbf{y}_p\}_{p=1}^{M_s N_{sc}}$, $\{\Psi_m\}_{m=1}^{M_s}$, L_p
- 2: **Normalize:** For each m , scale columns of Ψ_m to unit ℓ_2 -norm
- 3: **Initial:** $\mathcal{S} \leftarrow \emptyset$; $\mathbf{r}_p \leftarrow \mathbf{y}_p$ for $p = 1, \dots, M_s N_{sc}$
- 4: **for** $t = 0, \dots, L_p - 1$ **do**
- 5: **Score:** For each $g \in \{1, \dots, G_r G_t\}$,

$$S(g) = \sum_{p=1}^{M_s N_{sc}} \left| \Psi_{m(p)}(:, g)^H \mathbf{r}_p \right|^2$$
- 6: **Select:** $\hat{g} \leftarrow \arg \max_g S(g)$; $\mathcal{S} \leftarrow \mathcal{S} \cup \{\hat{g}\}$
- 7: **LS update (per snapshot):**
- 8: For each p , $\mathbf{A}_p = \Psi_{m(p)}(:, \mathcal{S})$, $\hat{\mathbf{h}}_p \leftarrow \arg \min_{\mathbf{x}} \|\mathbf{y}_p - \mathbf{A}_p \mathbf{x}\|_2^2 = \mathbf{A}_p^\dagger \mathbf{y}_p$, $\mathbf{r}_p \leftarrow \mathbf{y}_p - \mathbf{A}_p \hat{\mathbf{h}}_p$
- 9: **end for**
- 10: **Output:** Support $\hat{\mathcal{S}} = \{g_1, \dots, g_{L_p}\}$ and coefficients $\{\hat{\mathbf{h}}_p\}_{p=1}^{M_s N_{sc}}$

494 corresponding atoms can still be reliably detected by pooling
495 information from the remaining snapshots.

496 **5) Spatial-frequency estimation and mapping to angles.**
497 Recall from (12), (13) and (14) that the angular dictionary
498 is constructed as

$$\mathbf{\Gamma} = \mathbf{A}_r \otimes \mathbf{A}_t \in \mathbb{C}^{N_t N_r \times G_r G_t}, \quad (21)$$

499 where the transmit and receive dictionaries are defined as

$$\begin{aligned} \mathbf{A}_t &= [\mathbf{a}_t(\tilde{\boldsymbol{\mu}}_{t,1}), \dots, \mathbf{a}_t(\tilde{\boldsymbol{\mu}}_{t,G_t})], \\ \mathbf{A}_r &= [\mathbf{a}_r(\tilde{\boldsymbol{\mu}}_{r,1}), \dots, \mathbf{a}_r(\tilde{\boldsymbol{\mu}}_{r,G_r})], \end{aligned} \quad (22)$$

500 which sample the UPA steering vectors on a predefined
501 2D spatial-frequency grid $\{\tilde{\boldsymbol{\mu}}_{t,j}\}$ and $\{\tilde{\boldsymbol{\mu}}_{r,i}\}$. Hence, each
502 column index $g \in \{1, \dots, G_r G_t\}$ uniquely corresponds to a
503 pair $[i_r(g), i_t(g)]$ and, in turn, to a transmit/receive spatial-
504 frequency pair $(\tilde{\boldsymbol{\mu}}_{r,i_r(g)}, \tilde{\boldsymbol{\mu}}_{t,i_t(g)})$. Once the joint support $\hat{\mathcal{S}}$
505 is recovered, the spatial-frequency estimates for the l -th path
506 are obtained by searching the grid points as

$$\begin{aligned} \hat{\boldsymbol{\mu}}_{r,l} &= \tilde{\boldsymbol{\mu}}_{r,i_r(g_l)}, \\ \hat{\boldsymbol{\mu}}_{t,l} &= \tilde{\boldsymbol{\mu}}_{t,i_t(g_l)}. \end{aligned} \quad (23)$$

507 The spatial frequencies are related to the physical az-
508 imuth/elevation angles θ_x and θ_y , which can be evaluated
509 as

$$\begin{aligned} \mu_x &= \sin \theta_y \cos \theta_x, \\ \mu_y &= \cos \theta_y, \end{aligned} \quad (24)$$

510 under half-wavelength inter-element spacing. Therefore, the
511 BS-side AoA associated with the LoS atom \hat{g} can be recon-
512 structured from the estimated spatial-frequency vector $\hat{\boldsymbol{\mu}}_r$ by
513 inverting these relationships as follows:

$$\begin{aligned} \hat{\theta}_y &= \arccos(\hat{\mu}_y), \\ \hat{\theta}_x &= \text{atan2}\left(-\hat{\mu}_x, \sqrt{1 - \hat{\mu}_y^2}\right), \end{aligned} \quad (25)$$

514 where $\hat{\mu}_x$ and $\hat{\mu}_y$ denote the components of $\hat{\boldsymbol{\mu}}_r$. As shown
515 in Fig. 2, in the third stage, the modified BOMP algorithm

is employed for estimating the AoA and path gains based
on the MMV model constructed in the previous subsection.
More explicitly, across P snapshots, the modified BOMP
algorithm exploits the joint sparsity assumption in (17) and
selects the dominant angular atoms by maximizing the MMV
score in (18), followed by the per-snapshot LS update in (19).
The recovered coefficients are then mapped over the time-
frequency grid as in (20). The resultant unit-norm spatial-
frequency (or direction) vector $\hat{\boldsymbol{\mu}}_r$ will then be used in
Section III-C to form the BS-centered ray and, together with
the bistatic range constraint, to recover the UE position.

C. Residual Delay-Doppler Estimation and UE Position Recovery

Let $\hat{g} \in \hat{\mathcal{S}}$ denote the selected atom (e.g., the strongest LoS
when $l = 0$), and then collect its coefficients across (m, n)
into

$$\mathbf{S} \in \mathbb{C}^{M_s \times N_{sc}}, \quad [\mathbf{S}]_{m,n} = [\hat{\mathbf{h}}_{(m-1)N_{sc}+n}]_{\hat{g}}. \quad (26)$$

Afterwards, the upsampling delay-Doppler grids in the tem-
poral and frequency steering vectors are defined as $\mathcal{V} = \{v\}$
and $\mathcal{T} = \{\tau\}$ as $\mathbf{a}_t(v) = [e^{j2\pi t_m v}]_{m=1}^{M_s}$, $\mathbf{a}_f(\tau) =$
 $[e^{j2\pi f_n \tau}]_{n=1}^{N_{sc}}$. The 2D matched-filter response is

$$\mathbf{C}(v, \tau) = |\mathbf{a}_t(v)^H \mathbf{S} \mathbf{a}_f(\tau)|. \quad (27)$$

The residual estimates are obtained by the peak of \mathbf{C} as

$$(\hat{v}^{\text{res}}, \hat{\tau}^{\text{res}}) = \arg \max_{v \in \mathcal{V}, \tau \in \mathcal{T}} \mathbf{C}(v, \tau). \quad (28)$$

The spatial frequencies at the BS associated with \hat{g} is $\hat{\boldsymbol{\mu}}_r =$
 $[\hat{\mu}_x, \hat{\mu}_y, \hat{\mu}_z]^T$ with $\hat{\mu}_z = -\sqrt{\max(0, 1 - \hat{\mu}_x^2 - \hat{\mu}_y^2)}$. The UE
is assumed to lie along the ray $\mathbf{p}(s) = \mathbf{p}_{BS} + s \hat{\boldsymbol{\mu}}_r$, $s \geq 0$,
as depicted in Fig. 1. Let D denote the bistatic range implied
by the residual delay, represented as

$$D \triangleq \|\mathbf{p}_{LEO} - \mathbf{p}_{BS}\| + c \hat{\tau}^{\text{res}}. \quad (29)$$

The total distance satisfies the constraint

$$\zeta(s) \triangleq \|\mathbf{p}_{LEO} - \mathbf{p}(s)\| + s - D = 0. \quad (30)$$

We obtain a feasible $\hat{s} \geq 0$ by a 1-D search formulated as

$$\hat{s} = \arg \min_{s \in [0, 2D]} \zeta(s)^2, \quad (31)$$

and form the position candidate of the UE $\hat{\mathbf{p}} = \mathbf{p}_{BS} + \hat{s} \hat{\boldsymbol{\mu}}_r$.
As shown in the fourth stage of Fig. 2, the residual delay
 $\hat{\tau}^{\text{res}}$ and Doppler \hat{v}^{res} are estimated by (28), and the final
recovery of the UE's position is then estimated as the last
stage.

In summary, Fig. 1 presents the DL LEO-UE-BS bistatic
geometry and the TA/DPC intuition, while Fig. 2 trans-
lates this physical setup into the corresponding end-to-
end signal processing used for channel/angle estimation
and residual delay-Doppler aided localization. The pre-
compensated time-frequency observations are first cast into
a joint time-frequency-spatial MMV sparse model and
processed by a modified BOMP algorithm to estimate the
common angular support and path gains, after which a 2D
delay-Doppler matched filter is applied to obtain the residual

559 ToA/Doppler. The UE's position is finally recovered by
560 intersecting the estimated BS beam with the bistatic range.

561 **Remark:** It is worth noting that the proposed CS-based
562 framework possesses inherent robustness against multi-path
563 clutter. Since the channel is modeled as a sparse combination
564 of dictionary atoms, the separation of the target path from
565 clutter is achieved through atomic decomposition in the
566 joint time-frequency-spatial domain. Specifically, the greedy
567 recovery algorithm identifies paths based on their correlation
568 with the receive signal. In the scenario considered, the LEO-
569 UE-BS link typically acts as the dominant component having
570 the highest energy, attributed to the significant RCS of the
571 vehicular target relative to the weaker diffuse scattering from
572 environmental clutter. Therefore, the algorithm preferentially
573 selects the atom corresponding to the target's AoA and delay
574 in the initial iterations, effectively isolating the vehicular
575 UE's location from NLoS multi-path interference.

576 IV. Performance Evaluation

577 Again, we consider the LEO-UE-BS bistatic downlink trans-
578 mission shown in Fig. 1, where the positions of the LEO and
579 BS are $\mathbf{p}_{LEO} = [100, 200, 300]^T$ km with the satellite's
580 instant velocity of 7 km/s along the x-axis, and $\mathbf{p}_{BS} =$
581 $[-50, 190, 100]^T$ m, respectively. The location of the UE
582 is assumed to be the origin. The scatterers are randomly
583 generated between the UE and BS. Moreover, the carrier
584 frequency is set to $f_c = 28$ GHz, with subcarrier spacing of
585 $f_s = 120$ kHz, $c = 3 \times 10^8$ m/s, and using half-wavelength
586 element spacing. The number of antennas of the UPAs at
587 the LEO and BS are $N_t = N_{t,x}N_{t,y} = 4 \times 4 = 16$, $N_r =$
588 $N_{r,x}N_{r,y} = 4 \times 4 = 16$. Furthermore, $G_r = G_t = G \times G$,
589 where G is the number of quantization levels for both $N_{t,x}$
590 and $N_{t,y}$ or $N_{r,x}$ and $N_{r,y}$. We assume a vehicular target
591 with an RCS of $\sigma_{RCS} \approx 100$ m² (20 dBsm), which is
592 consistent with empirical measurements for multi-passenger
593 vehicles at Ka-band [47]². The receive signal-to-noise ratio
594 (SNR) is defined as $\mathbb{E} \left\{ \|\tilde{\mathbf{y}}_{m,n}\|_2^2 \right\} / \mathbb{E} \left\{ \|\mathbf{z}_{m,n}\|_2^2 \right\}$, averaged
595 over P time-frequency snapshots within a pilot frame, which
596 results in processing gain by stacking P snapshots via MMV
597 support recovery and 2D matched filtering. The number of
598 Monte Carlo trials is set to 1500.

599 The benchmarks considered in this paper include 1)
600 oracle-least square (LS), 2) orthogonal matching pursuit
601 (OMP) with single measurement vector (SMV) [49], 3)
602 linear minimum mean square error (LMMSE), 4) com-
603 pressed sampling matching pursuit (CoSaMP) [50] and 5)
604 approximate message passing (AMP) [51], [52]. The com-
605 plexity of these algorithms is summarized in Table 3, where
606 T_{CoSaMP} , T_{AMP} , T_{LMMSE} denote the number of iterations
607 for the different algorithms. Note that the LMMSE estimator
608 relies on the conjugate gradient algorithm, which avoids

²To justify the physical feasibility of the bistatic link at 28 GHz, we assume a Ka-band LEO satellite having an EIRP of 43.1 dBW [48]. For instance, for a vehicular UE associated with an effective RCS of 20 dBsm located 300 km from the LEO and 50 m from the BS, the receive power is approximately -106 dBm with the receive antenna gain of 16 dBi. When considering a noise power of -108 dBm, the receive SNR is 1.5 dB.

TABLE 3: Computational Complexity Comparison of Different Algorithms

Algorithms	Computational complexity
Oracle-LS	$\mathcal{O}(M_s N_{sc} N_{rf})$
OMP-SMV	$\mathcal{O}(N_{rf} G_r G_t) + \mathcal{O}(M_s N_{sc} N_{rf})$
CoSaMP-SMV	$\mathcal{O}(2T_{\text{CoSaMP}} N_{rf} G_r G_t) + \mathcal{O}(M_s N_{sc} N_{rf})$
Proposed	$\mathcal{O}(M_s N_{sc} N_{rf} G_r G_t)$
LMMSE	$\mathcal{O}(2M_s N_{sc} T_{\text{LMMSE}} N_{rf} G_r G_t)$
AMP-MMV	$\mathcal{O}(2T_{\text{AMP}} M_s N_{sc} N_{rf} G_r G_t)$

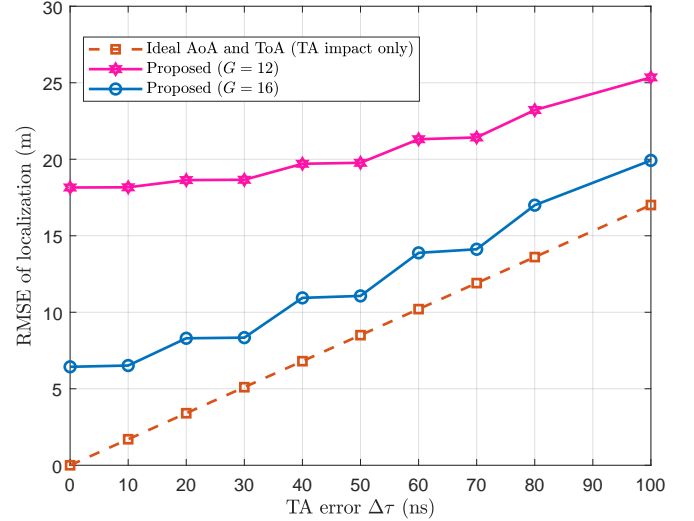


FIGURE 3: RMSE performance of localization accuracy versus different TA errors, when $M_s = 8$, $N_{sc} = 32$ and SNR=0 dB.

609 explicit inversion of the $(G_r G_t \times G_r G_t)$ -element covariance
610 matrix, and each iteration only requires two matrix-vector
611 multiplications with the sensing matrix and its Hermitian.

612 The estimation performance is characterized by the root
613 mean squared error (RMSE), defined as:

$$614 \text{RMSE} = \sqrt{\frac{1}{k_{\text{monte}}} \sum_{k_{\text{monte}}=1}^{K_{\text{monte}}} \|\hat{\mathbf{q}}_{k_{\text{monte}}} - \mathbf{q}_{k_{\text{monte}}}\|_2^2}, \quad (32)$$

615 where K denotes the number of Monte Carlo trials, and \mathbf{q}
616 and $\hat{\mathbf{q}}$ are the true and estimated values, respectively.

617 Fig. 3 illustrates the impact of the TA error $\Delta\tau$ on the
618 localization RMSE for different beamspace resolutions. It
619 is worth noting that $\Delta\tau$ essentially reflects the potential
620 errors in the prior LEO-BS geometry information and syn-
621 chronization mismatches. The dashed curve represents the
622 geometric lower bound obtained when the AoA/AoD and
623 residual ToA are assumed to be perfectly estimated and only
624 the TA mismatch is propagated through the bistatic ellipse.
625 As expected, this RMSE trend evolves almost linearly with
626 $\Delta\tau$, indicating that a small synchronization error in the LEO-
627 BS reference link gradually aggravates the position bias. Furthermore, the proposed scheme follows this trend with

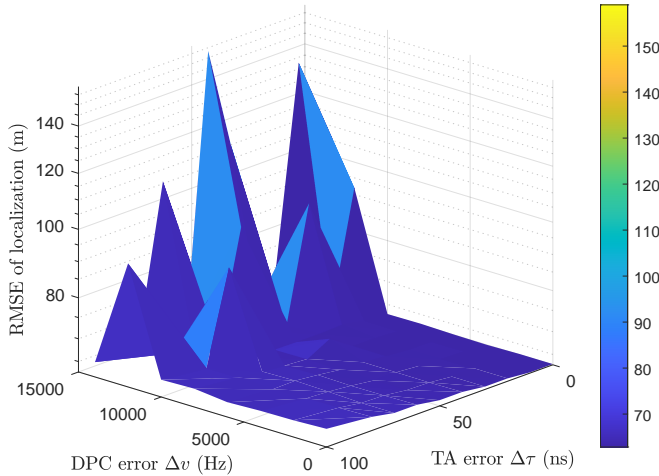


FIGURE 4: The RMSE performance of localization accuracy versus different TA and DPC errors, when we have $M_s = 32$, $N_{sc} = 32$ and SNR= 0 dB.

628 a near-constant gap of only a few meters, which indicates
 629 that the main performance degradation is imposed by the
 630 TA misalignment, rather than by the compressed sensing
 631 estimation itself for a sufficiently fine beamspace grid. In
 632 particular, for $\Delta\tau \leq 40$ ns, the proposed scheme still
 633 achieves sub-10 m RMSE, yielding a reasonable robustness
 634 to moderate TA errors. By contrast, when the angular grid is
 635 coarser ($G = 12$), the RMSE increased to about 18-25 m for
 636 $\Delta\tau < 100$ ns. This confirms that in the coarse-grid regime,
 637 the localization accuracy is mainly limited by the beamspace
 638 angular quantization error, and any further refinement of the
 639 TA/DPC yields marginal benefits.

640 Fig. 4 shows the localization sensitivity to TA residual
 641 error $\Delta\tau$ and DPC error Δv , when we set $M_s = 32$,
 642 $N_{sc} = 32$, and SNR= 0 dB. From the simulation results
 643 in Fig. 4, we conclude that after the TA pre-compensation,
 644 moderate residual TA errors mainly introduce a mild bias in
 645 the residual delay estimate and do not fundamentally break
 646 the angle-delay association. By contrast, the RMSE becomes
 647 highly sensitive to the DPC mismatch for $\Delta v > 5$ kHz.
 648 This behavior is consistent with a Doppler-mismatch effect,
 649 where the residual Doppler induces symbol-to-symbol phase
 650 rotation and the loss of coherent combining across the M_s
 651 pilot symbols, which shifts the matched filter response in
 652 the delay-Doppler domain. Therefore, a wrong bistatic range
 653 estimate is employed to recover the target’s location, and
 654 thus causes a large positioning error, even though the final
 655 geometric solver only uses the residual delay. Therefore, the
 656 residual Doppler estimation is necessary for reliable delay
 657 extraction and corresponding localization.

658 To evaluate the trade-off between hardware complexity
 659 (number of RF chains, denoted as N_{rf}) and beamspace res-
 660 olution G , Fig. 5 presents the localization RMSE versus SNR
 661 for various combinations of $N_{rf} \in \{8, 16\}$ and quantization
 662 levels $G \in \{8, 12, 16\}$. Observed in Fig. 5 that when the
 663 number of quantization levels G is increased, which means
 664 that the beamspace resolution increases, the estimation of

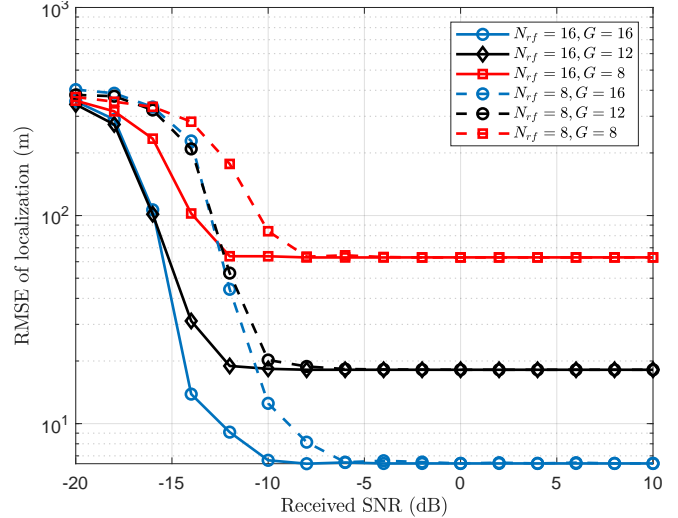


FIGURE 5: The RMSE performance of localization accuracy with different angular quantization levels, when $M_s = 8$ and $N_{sc} = 32$.

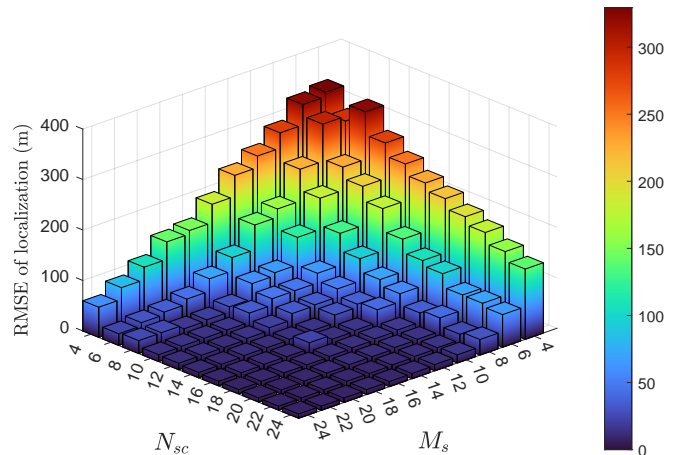


FIGURE 6: The RMSE performance of localization accuracy with different M_s and N_{sc} , when $N_{rf} = 4$, $G = 16$ and SNR = -6 dB.

665 the AoA and the residual delay becomes more accurate.
 666 Specifically, the localization accuracy can be improved from
 667 about 60 meters to about 6 meters by increasing G from 8 to
 668 16. Furthermore, when N_{rf} is increased from 8 to 16, there
 669 is a further 4 dB gain at SNR=-6 dB, concluding that higher
 670 hardware complexity results in better beamforming gain and
 671 MMV recovery even under the same angular resolution.

672 Next, we investigate the impact of pilot overhead in Fig. 6.
 673 The specific grid of M_s and N_{sc} values are chosen to
 674 illustrate the effect of the joint time-frequency diversity gain
 675 on the estimation accuracy. Explicitly, Fig. 6 highlights the
 676 benefit of increasing the time-frequency pilot overhead. In-
 677 creasing M_s improves Doppler estimation, while increasing
 678 N_{sc} improves the delay estimation. Their combined benefit
 679 reduces the positioning error roughly in line with the product

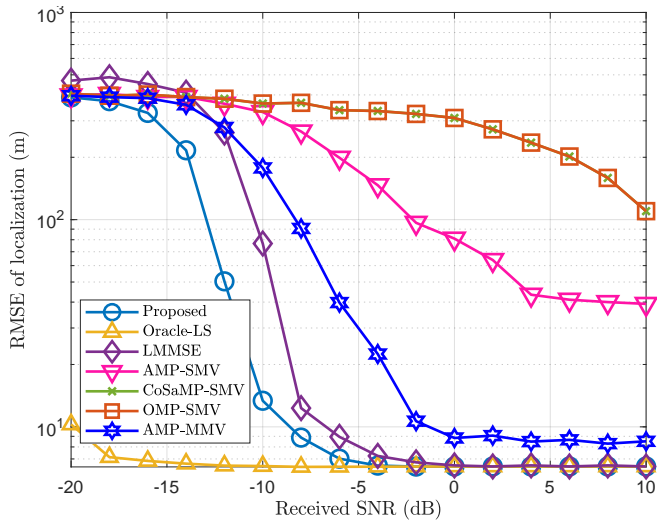


FIGURE 7: The RMSE performance of localization accuracy with different compressed sensing algorithms, when we set $M_s = 8$, $N_{sc} = 32$, $N_{rf} = 8$, and $G = 16$.

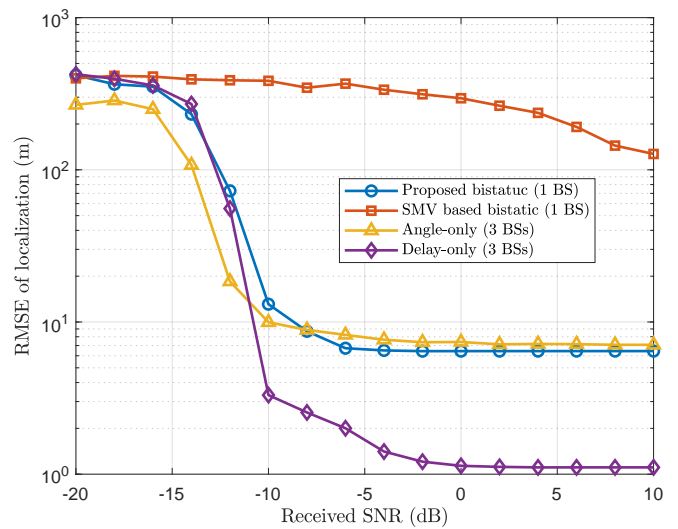


FIGURE 8: The RMSE performance of localization accuracy versus different localization baselines.

of $M_s N_{sc}$. Furthermore, the channel estimation performance also improves with more snapshots. Moreover, it can be observed that the localization accuracy is more sensitive to M_s , which is because a higher M_s improves training diversity in (15), leading to better MMV conditions.

Fig. 7 compares the localization accuracy against the state-of-the-art channel estimation algorithms. To ensure a fair comparison, we fix the system parameters to a representative operating point ($M_s = 8, N_{sc} = 32, N_{rf} = 8, G = 16$), which balances resource consumption and potential accuracy. The Oracle-LS curve provides an upper performance bound, since it assumes perfect knowledge of the true support and only estimates the path coefficients. Hence its high-SNR behavior is almost flat and it is mainly limited by the AoA/AoD and delay/Doppler grid quantization. The proposed joint MMV scheme exhibits a threshold around $\text{SNR} = -6$ dB and then rapidly converges to the Oracle-LS floor, confirming that fully exploiting the joint sparsity across all time-frequency snapshots is highly beneficial for localization. The LMMSE exhibits a estimator residual RMSE. However, as seen in Fig. 7, the global shrinkage of its coefficients leads to less reliable support selection at low SNR than the proposed solution. In AMP-SMV, the AMP algorithm is run independently for each OFDM symbol, so the snapshots are processed separately and no joint intersymbol sparsity is exploited. Its performance improves only gradually with the SNR and remains clearly inferior to the proposed scheme. By contrast, AMP-MMV jointly processes all OFDM symbols under a common-support based MMV model, which yields a noticeable SNR gain and allows it to approach the oracle floor. However, a small gap persists because AMP is sensitive to the highly coherent, structured sensing matrix adopted in our beamspace formulation. Finally, the single-snapshot OMP-SMV and CoSaMP-SMV

algorithms do not exploit any joint sparsity. Consequently, they exhibit the highest RMSE over the entire SNR range.

Fig. 8 compares the proposed pipeline against three different positioning baselines, such as a SMV based bistatic AoA and ToA based estimator, an angle-only estimator, and a delay-only estimator. These baselines are standard in localization studies because they clarify whether the performance gain originates from more reliable angle inference, more accurate delay inference, or their joint exploitation under bistatic geometry. Specifically, the proposed MMV-based method exhibits a sharp RMSE reduction as the receive SNR increases from -15 dB to -10 dB, followed by a stable error floor in the high SNR region. This behavior is expected because the proposed method estimates AoA/AoD from a discrete beamspace dictionary, and the residual angular grid mismatch dominates the high-SNR regime once the delay estimate becomes sufficiently accurate. In contrast, the SMV based method remains significantly worse across the entire SNR range. Compared to other baselines, this SMV based method does not exploit time-frequency diversity and is thus more sensitive to noise and NLoS components, which increases the probability of dominant-path mis-selection and yields biased AoA/ToA estimates. Moreover, the angle-only baseline based on three BSs improves markedly over the SMV based method and achieves a meter-level floor for $\text{SNR} > -6$ dB. This trend indicates that after noise becomes less dominant, the achievable accuracy is primarily limited by the angular resolution of the adopted beamspace grid. The delay-only baseline based on the ToA multilateration of 3 BSs achieves the lowest RMSE and converges close to the meter-level regime at high SNR. This improvement is mainly due to the stronger geometric observability enabled by multi-BS diversity and the averaging effect across independent ToA estimates.

Fig. 9 depicts the computational complexity evaluated from the equations in Table 3. In each subplot, only one

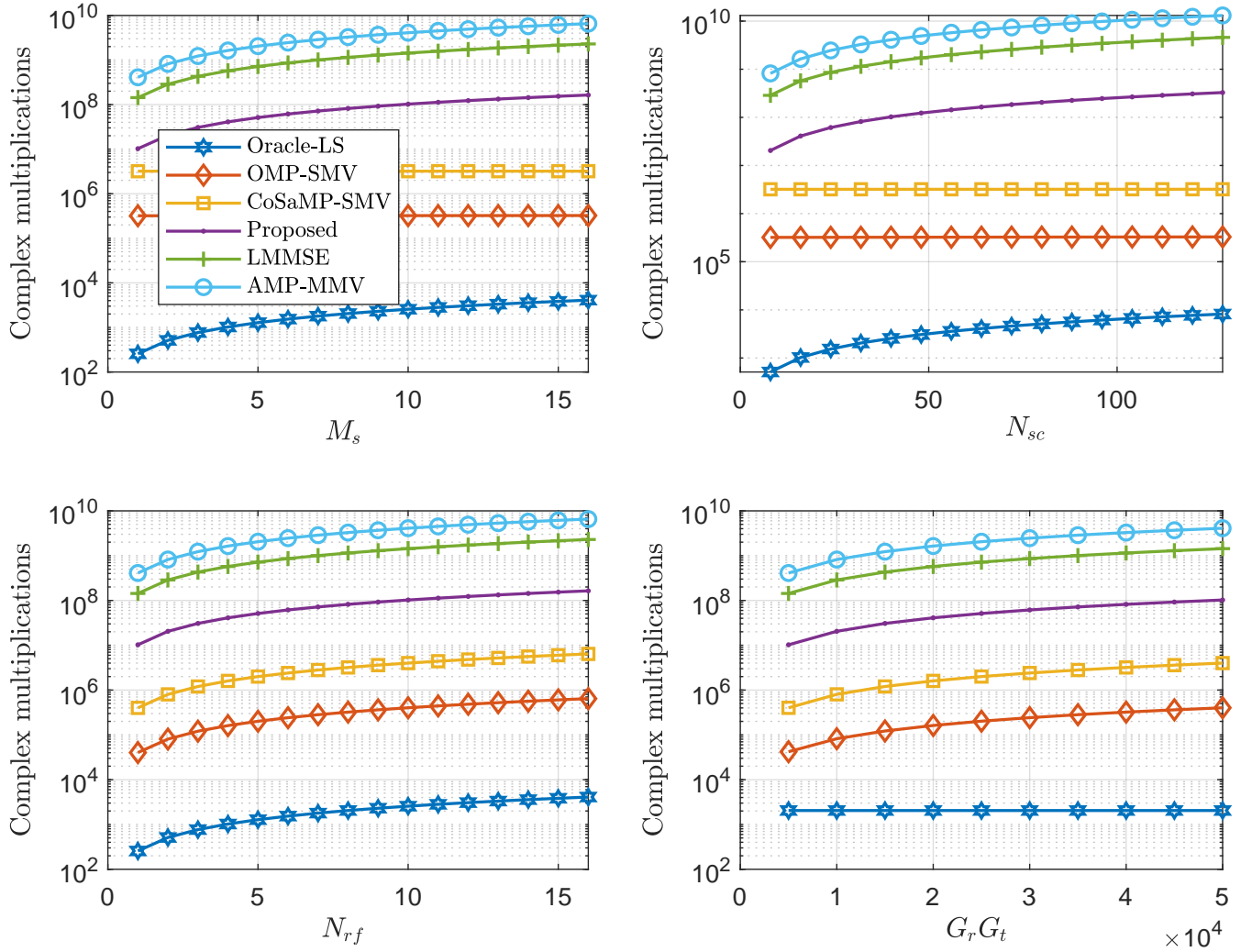


FIGURE 9: The comparison of different algorithms, including Oracle-LS, OMP-SMV, CoSaMp-SMV, LMMSE, AMP-MMV, and our proposed algorithm: The computational complexity versus the different parameters M_s , N_{sc} , N_{rf} , and $G_r G_t$.

parameter is varied while the others are fixed to $M_s = 8$, $N_{sc} = 32$, $N_{rf} = 8$, and $G_r G_t = 4 \times 10^4$. The iteration numbers are set to $T_{\text{CoSaMP}} = 5$, $T_{\text{LMMSE}} = 7$, and $T_{\text{AMP}} = 20$. In all cases the Oracle-LS benchmark exhibits the lowest complexity, since it only performs a single least-squares update over the $M_s N_{sc} N_{rf}$ unknown coefficients. The OMP-SMV and CoSaMP-SMV algorithms incur a moderate cost that is dominated by the complexity term of $\mathcal{O}(N_{rf} G_r G_t)$ and $\mathcal{O}(2T_{\text{CoSaMP}} N_{rf} G_r G_t)$, respectively. This trend prevails G is significantly higher than $M_s N_{sc}$, and therefore their curves remain almost flat when M_s or N_{sc} increases, while growing approximately linearly with N_{rf} and the beamspace grid size G . By contrast, the proposed joint MMV estimator, the LMMSE method and AMP-MMV all scale with the full four-dimensional product $M_s N_{sc} N_{rf} G$, and thus their complexity increases roughly linearly with each of these parameters. Among these, the proposed scheme lies between the low-complexity greedy

approaches, while the iterative methods of the LMMSE and AMP-MMV algorithms exhibit the highest complexity because each iteration requires two matrix-vector products over the entire beamspace grid. Therefore, their total cost grows proportionally with the respective number of iterations T_{LMMSE} and T_{AMP} .

V. Conclusions

A bistatic localization system using hybrid beamforming with a sparse MMV formulation was proposed. Specifically, a modified BOMP algorithm was conceived for recovering the angular information, while a 2D matched filter was employed for estimating the residual delay and Doppler. Furthermore, an elliptic constraint is used for recovering the UE position. The results show consistent gains for increased pilot in time- and frequency-domain, and also angular resolution. The results indicate that the proposed scheme is capable of achieving meter-level accuracy for LEO-assisted downlink

785 localization scenarios. As an important direction for future
 786 work, it is of interest to relax the strictly orthogonal pilot
 787 allocation assumed in this paper and to investigate more
 788 general non-orthogonal pilot settings, where the resultant
 789 multi-user interference and pilot contamination must be
 790 explicitly taken into account.

791 REFERENCES

- 792 [1] G. Geraci, D. López-Pérez, M. Benzaghta, and S. Chatzinotas, "Integrating terrestrial and non-terrestrial networks: 3D opportunities and challenges," *IEEE Communications Magazine*, vol. 61, no. 4, pp. 42–48, 2023.
- 793 [2] E. Erdogan, O. B. Yahia, G. K. Kurt, and H. Yanikomeroglu, "Optical HAPS eavesdropping in vertical heterogeneous networks," *IEEE Open Journal of Vehicular Technology*, vol. 4, pp. 208–216, 2023.
- 794 [3] J. Liang, A. U. Chaudhry, E. Erdogan, H. Yanikomeroglu, G. K. Kurt, P. Hu, K. Ahmed, and S. Martel, "Free-space optical (FSO) satellite networks performance analysis: Transmission power, latency, and outage probability," *IEEE Open Journal of Vehicular Technology*, vol. 5, pp. 244–261, 2023.
- 795 [4] H. Zheng, M. Atia, and H. Yanikomeroglu, "Realistic channel and delay coefficient generation for dual mobile space-ground links: A tutorial," *IEEE Open Journal of Vehicular Technology*, vol. 5, pp. 762–777, 2024.
- 796 [5] H. K. Dureppagari, C. Saha, H. S. Dhillon, and R. M. Buehrer, "NTN-based 6G localization: Vision, role of LEOs, and open problems," *IEEE Wireless Communications*, vol. 30, no. 6, pp. 44–51, 2023.
- 797 [6] K. Li, M. El-Hajjar, and L.-l. Yang, "Millimeter-wave based localization using a two-stage channel estimation relying on few-bit ADCs," *IEEE Open Journal of the Communications Society*, vol. 2, pp. 1736–1752, 2021.
- 798 [7] Z. Z. M. Kassas, J. Khalife, K. Shamaei, and J. Morales, "I hear, therefore I know where I am: Compensating for GNSS limitations with cellular signals," *IEEE Signal Processing Magazine*, vol. 34, no. 5, pp. 111–124, 2017.
- 799 [8] J. A. del Peral-Rosado, R. Raulefs, J. A. López-Salcedo, and G. Seco-Granados, "Survey of cellular mobile radio localization methods: From 1G to 5G," *IEEE Communications Surveys & Tutorials*, vol. 20, no. 2, pp. 1124–1148, 2018.
- 800 [9] M. Kayton, "Global positioning system: signals, measurements, and performance [Book Review]," *IEEE Aerospace and Electronic Systems Magazine*, vol. 17, no. 10, pp. 36–37, 2002.
- 801 [10] C. Zhang, Q. Li, C. Xu, L.-L. Yang, and L. Hanzo, "Space-air-ground integrated networks: Their channel model and performance analysis," *IEEE Open Journal of Vehicular Technology*, vol. 6, pp. 1501–1523, May 2025.
- 802 [11] H. K. Dureppagari, C. Saha, H. Krishnamurthy, X. Wang, A. Rico-Alvarino, R. M. Buehrer, and H. S. Dhillon, "LEO-based positioning: Foundations, signal design, and receiver enhancements for 6G NTN," *IEEE Communications Magazine*, vol. 63, no. 11, pp. 130–137, 2025.
- 803 [12] P. Angeletti and R. De Gaudenzi, "A pragmatic approach to massive MIMO for broadband communication satellites," *IEEE Access*, vol. 8, pp. 132212–132236, 2020.
- 804 [13] M. M. Azari, S. Solanki, S. Chatzinotas, O. Kodheli, H. Sallouha, A. Colpaert, J. F. M. Montoya, S. Pollin, A. Haqiqatnejad, A. Mostaani *et al.*, "Evolution of non-terrestrial networks from 5G to 6G: A survey," *IEEE communications surveys & tutorials*, vol. 24, no. 4, pp. 2633–2672, 2022.
- 805 [14] G. Araniti, A. Iera, S. Pizzi, and F. Rinaldi, "Toward 6G non-terrestrial networks," *IEEE Network*, vol. 36, no. 1, pp. 113–120, 2021.
- 806 [15] X. Zhu and C. Jiang, "Integrated satellite-terrestrial networks toward 6G: Architectures, applications, and challenges," *IEEE Internet of Things Journal*, vol. 9, no. 1, pp. 437–461, 2021.
- 807 [16] I. S. Mohamad Hashim and A. Al-Hourani, "Satellite-based localization of IoT devices using joint Doppler and angle-of-arrival estimation," *Remote Sensing*, vol. 15, no. 23, p. 5603, 2023.
- 808 [17] A. K. Meshram, S. Kumar, J. Querol, and S. Chatzinotas, "Doppler effect mitigation in LEO-based 5G non-terrestrial networks," in *2023 IEEE Globecom Workshops (GC Wkshps)*. IEEE, 2023, pp. 311–316.
- 809 [18] B.-H. Yeh, J.-M. Wu, and R. Y. Chang, "Efficient Doppler compensation for LEO satellite downlink OFDMA systems," *IEEE Transactions on Vehicular Technology*, vol. 73, no. 12, pp. 18863–18877, 2024.
- 810 [19] L. You, X. Qiang, Y. Zhu, F. Jiang, C. G. Tsinos, W. Wang, H. Wymeersch, X. Gao, and B. Ottersten, "Integrated communications and localization for massive MIMO LEO satellite systems," *IEEE Transaction. Wireless Commun.*, vol. 23, no. 9, pp. 11061–11075, Sep. 2024.
- 811 [20] M. Alsenwi, E. Lagunas, and S. Chatzinotas, "Robust beamforming for massive MIMO LEO satellite Communications: A risk-aware learning framework," *IEEE Transactions on Vehicular Technology*, vol. 73, no. 5, pp. 6560–6571, 2024.
- 812 [21] J. Khalife, M. Neinaivaie, and Z. M. Kassas, "Blind Doppler tracking from OFDM signals transmitted by broadband LEO satellites," in *2021 IEEE 93rd Vehicular Technology Conference (VTC2021-Spring)*, 2021, pp. 1–5.
- 813 [22] D.-R. Emenonye, H. S. Dhillon, and R. Michael Buehrer, "Fundamentals of LEO-based localization," *IEEE Transactions on Information Theory*, vol. 71, no. 7, pp. 5277–5311, 2025.
- 814 [23] K. Li, M. El-Hajjar, and L.-L. Yang, "Reconfigurable intelligent surface aided position and orientation estimation based on joint beamforming with limited feedback," *IEEE Open Journal of the Communications Society*, vol. 4, pp. 748–767, 2023.
- 815 [24] K.-X. Li, X. Gao, and X.-G. Xia, "Channel estimation for LEO satellite massive MIMO OFDM communications," *IEEE Transactions on Wireless Communications*, vol. 22, no. 11, pp. 7537–7550, 2023.
- 816 [25] Z. Zhang, Y. Li, C. Huang, Q. Guo, L. Liu, C. Yuen, and Y. L. Guan, "User activity detection and channel estimation for grant-free random access in LEO satellite-enabled Internet of Things," *IEEE Internet of Things Journal*, vol. 7, no. 9, pp. 8811–8825, 2020.
- 817 [26] K. Li, J. He, M. El-Hajjar, and L.-L. Yang, "Localization in reconfigurable intelligent surface aided mmwave systems: A multiple measurement vector based channel estimation method," *IEEE Transactions on Vehicular Technology*, vol. 73, no. 9, pp. 13326–13339, 2024.
- 818 [27] K. Li, M. El-Hajjar, C. Xu, and L. Hanzo, "Indoor localization and tracking in reconfigurable intelligent surface aided mmwave systems," *IEEE Open Journal of Vehicular Technology*, vol. 6, pp. 1815–1831, 2025.
- 819 [28] X. Wang, W. Shen, C. Xing, J. An, and L. Hanzo, "Joint Bayesian channel estimation and data detection for OTFS systems in LEO satellite communications," *IEEE Transactions on Communications*, vol. 70, no. 7, pp. 4386–4399, 2022.
- 820 [29] T. Yue, A. Liu, and X. Liang, "Block-based Kalman channel tracking for LEO satellite communication with massive MIMO," *IEEE Communications Letters*, vol. 27, no. 2, pp. 645–649, 2022.
- 821 [30] H. Griffiths and A. Farina, "Multistatic and networked radar: Principles and practice," in *2021 IEEE Radar Conference (RadarConf21)*. IEEE, 2021, pp. 1–5.
- 822 [31] C. B. Barneto, T. Riihonen, M. Turunen, L. Anttila, M. Fleischer, K. Stadius, J. Ryyänen, and M. Valkama, "Full-duplex OFDM radar with LTE and 5G NR waveforms: Challenges, solutions, and measurements," *IEEE Transactions on Microwave Theory and Techniques*, vol. 67, no. 10, pp. 4042–4054, 2019.
- 823 [32] A. Bazzi and M. Chaffi, "Low dynamic range for RIS-aided bistatic integrated sensing and communication," *IEEE Journal on Selected Areas in Communications*, vol. 43, no. 3, pp. 912–927, 2025.
- 824 [33] Z. Han, H. Ding, L. Han, L. Ma, X. Zhang, M. Lou, Y. Wang, J. Jin, Q. Wang, G. Liu *et al.*, "Cellular network based multistatic integrated sensing and communication systems," *IET Communications*, vol. 18, no. 20, pp. 1878–1888, 2024.
- 825 [34] J. Park, J. Seong, Y. Mao, W. Shin, and B. Ottersten, "A bistatic ISAC framework for LEO satellite systems: A rate-splitting approach," *IEEE Transactions on Aerospace and Electronic Systems*, vol. 61, no. 6, pp. 17282–17301, 2025.
- 826 [35] J. Park, J. Seong, J. Ryu, Y. Mao, and W. Shin, "RSMA-based bistatic ISAC framework for LEO satellite systems," in *2024 IEEE International Conference on Communications Workshops (ICC Workshops)*. IEEE, 2024, pp. 1840–1845.
- 827 [36] X. Li, B. Shang, and Q. Wu, "A bistatic sensing system in space-air-ground integrated networks," in *2024 IEEE/CIC International Conference on Communications in China (ICCC)*. IEEE, 2024, pp. 1823–1827.
- 828 [37] X. Lin, Z. Lin, S. E. Löwenmark, J. Rune, R. Karlsson *et al.*, "Doppler shift estimation in 5G new radio non-terrestrial networks," in *2021 IEEE Global Communications Conference (GLOBECOM)*. IEEE, 2021, pp. 1–6.
- 829 [38] E. F. Knott, J. F. Schaeffer, and M. T. Tulley, *Radar cross section*. SciTech Publishing, 2004.
- 830 [39] J. Li, Y. Zhang, Y. Zhang, W. Xiong, Y. Huang, and Z. Wang, "Fast tracking Doppler compensation for OFDM-based LEO satellite data transmission," in *2016 2nd IEEE International Conference on Computer and Communications (ICCC)*. IEEE, 2016, pp. 1814–1817.
- 831 [40] L. Rothman, *et al.*, "The HITRAN2012 molecular spectroscopic database," *J. Quant. Spectrosc. Radiat. Transfer.*, vol. 130, pp. 936

937 4–50, 2013, HITRAN2012 special issue. [Online]. Available: <https://www.sciencedirect.com/science/article/pii/S0022407313002859>

938

939 [41] J. Jose, A. Ashikhmin, T. L. Marzetta, and S. Vishwanath, “Pilot

940 contamination and precoding in multi-cell TDD systems,” *IEEE Trans-*

941 *actions on Wireless Communications*, vol. 10, no. 8, pp. 2640–2651,

942 2011.

943 [42] H. Yin, D. Gesbert, M. Filippou, and Y. Liu, “A coordinated approach

944 to channel estimation in large-scale multiple-antenna systems,” *IEEE*

945 *Journal on selected areas in communications*, vol. 31, no. 2, pp. 264–

946 273, 2013.

947 [43] M. Ke, Z. Gao, Y. Wu, X. Gao, and R. Schober, “Compressive sensing-

948 based adaptive active user detection and channel estimation: Massive

949 access meets massive MIMO,” *IEEE transactions on signal processing*,

950 vol. 68, pp. 764–779, 2020.

951 [44] K. Senel and E. G. Larsson, “Grant-free massive MTC-enabled mas-

952 sive MIMO: A compressive sensing approach,” *IEEE Transactions on*

953 *Communications*, vol. 66, no. 12, pp. 6164–6175, 2018.

954 [45] F. Liu, Y. Cui, C. Masouros, J. Xu, T. X. Han, Y. C. Eldar, and

955 S. Buzzi, “Integrated sensing and communications: Toward dual-

956 functional wireless networks for 6G and beyond,” *IEEE journal on*

957 *selected areas in communications*, vol. 40, no. 6, pp. 1728–1767, 2022.

958 [46] W. Wang, T. Chen, R. Ding, G. Seco-Granados, L. You, and X. Gao,

959 “Location-based timing advance estimation for 5G integrated LEO

960 satellite communications,” *IEEE Transactions on Vehicular Technol-*

961 *ogy*, vol. 70, no. 6, pp. 6002–6017, 2021.

962 [47] I. Matsunami, R. Nakamura, and A. Kajiwara, “RCS measurements for

963 vehicles and pedestrian at 26 and 79GHz,” in *2012 6th International*

964 *Conference on Signal Processing and Communication Systems*. IEEE,

965 2012, pp. 1–4.

966 [48] G. Amendola, D. Cavallo, T. Chaloun, N. Defrance, G. Goussetis,

967 M. Margalef-Rovira, E. Martini, O. Quevedo-Teruel, V. Valenta, N. J.

968 Fonseca *et al.*, “Low-earth orbit user segment in the Ku and Ka-

969 band: An overview of antennas and RF front-end technologies,” *IEEE*

970 *Microwave Magazine*, vol. 24, no. 2, pp. 32–48, 2023.

971 [49] J. A. Tropp and A. C. Gilbert, “Signal recovery from random mea-

972 surements via orthogonal matching pursuit,” *IEEE Transactions on*

973 *information theory*, vol. 53, no. 12, pp. 4655–4666, 2007.

974 [50] D. Needell and J. A. Tropp, “CoSaMP: Iterative signal recovery

975 from incomplete and inaccurate samples,” *Applied and computational*

976 *harmonic analysis*, vol. 26, no. 3, pp. 301–321, 2009.

977 [51] S. Rangan, “Generalized approximate message passing for estimation

978 with random linear mixing,” in *2011 IEEE International Symposium*

979 *on Information Theory Proceedings*. IEEE, 2011, pp. 2168–2172.

980 [52] L. Liu and W. Yu, “Massive connectivity with massive MIMO—Part I:

981 Device activity detection and channel estimation,” *IEEE Transactions*

982 *on Signal Processing*, vol. 66, no. 11, pp. 2933–2946, 2018.



Kunlun Li (Member, IEEE) received his M.Sc and PhD degrees in wireless communications from the University of Southampton, U.K. in 2018 and 2024, respectively, where he is a research fellow with the Next Generation Wireless Research Group. His research interests include millimeter-wave, channel estimation, integrated sensing and communications (ISAC) and reconfigurable intelligent surface for wireless positioning and communications.



Chao Zhang (Member, IEEE) received his B.S. degree in Electrical Engineering from the Southwest University, China, in 2018, and received his Ph.D. degree in Electrical Engineering from Queen Mary University of London, U.K., in 2024. He is currently a Research Fellow with the School of Electronics and Computer Science, University of Southampton, Southampton, U.K. His research interests include the channel modelling and performance analysis of stochastic-geometry-based networks, including non-orthogonal multiple access, grant-free transmission, reconfigurable intelligent surface, and integrated sensing and communications. His current research interest is on space-air-ground integrated networks.



Mohammed El-Hajjar (Senior Member, IEEE) is a Professor of Signal Processing for Wireless Communications in the School of Electronics and Computer Science in the University of Southampton. He is the recipient of several academic awards and has published a Wiley-IEEE book and more than 150 IEEE journal and conference papers and in excess of 10 patents. Mohammed’s research interests include the design of intelligent and energy efficient transceivers, millimeter wave communications and localisation, and machine learning for wireless communications. Mohammed’s research is funded by the Engineering and Physical Sciences Research Council, the Royal Academy of Engineering and many industrial partners.



CHAO XU (Senior Member, IEEE) received the B.Eng. degree in telecommunications from Beijing University of Posts and Telecommunications, Beijing, China, the B.Sc. (Eng.) degree (with First Class Hons.) in telecommunications from the Queen Mary, University of London, London, U.K., through a Sino-U.K. joint degree Program in 2008, and the M.Sc. degree (with Distinction) in radio frequency communication systems and the Ph.D. degree in wireless communications from the University of Southampton, Southampton, U.K., in 2009 and 2015, respectively. He is currently a Senior Lecturer with Next Generation Wireless Research Group, University of Southampton. His research interests include index modulation, reconfigurable intelligent surfaces, noncoherent detection, and turbo detection. He was the recipient of the Best M.Sc. Student in Broadband and Mobile Communication Networks by the IEEE Communications Society United Kingdom and Republic of Ireland Chapter in 2009, 2012 Chinese Government Award for Outstanding Self-Financed Student Abroad, 2017 Dean’s Award, Faculty of Physical Sciences and Engineering, University of Southampton, 2023 Marie Skłodowska-Curie Actions Global Postdoctoral Fellowships with the highest evaluation score of 100/100.



Lajos Hanzo (Life Fellow, IEEE) received Honorary Doctorates from the Technical University of Budapest (2009) and Edinburgh University (2015). He is a Foreign Member of the Hungarian Science-Academy, Fellow of the Royal Academy of Engineering (FREng), of the IET, of EURASIP. He holds the IEEE Edwin Howard Armstrong Award and the IEEE Eric Summer Technical Field Award. For further details please see <http://www-mobile.ecs.soton.ac.uk>, https://en.wikipedia.org/wiki/Lajos_Hanzo.